

## Analysis of the Global Microwave Polarization Data of Clouds

XIPING ZENG,<sup>a,b</sup> GAIL SKOFRONICK-JACKSON,<sup>b</sup> LIN TIAN,<sup>b,c</sup> AMBER E. EMORY,<sup>b</sup>  
WILLIAM S. OLSON,<sup>b,d</sup> AND RACHAEL A. KROODSMA<sup>e,f</sup>

<sup>a</sup> Atmospheric Modeling Branch, U.S. Army Research Laboratory, Adelphi, Maryland

<sup>b</sup> Mesoscale Atmospheric Processes Laboratory, NASA Goddard Space Flight Center, Greenbelt, Maryland

<sup>c</sup> Goddard Earth Sciences Technology and Research, Morgan State University, Baltimore, Maryland

<sup>d</sup> Joint Center for Earth Systems Technology, University of Maryland, Baltimore, Baltimore, Maryland

<sup>e</sup> Earth System Science Interdisciplinary Center, University of Maryland, College Park, College Park, Maryland

<sup>f</sup> Precipitation Processing System, NASA Goddard Space Flight Center, Greenbelt, Maryland

(Manuscript received 11 May 2018, in final form 21 August 2018)

### ABSTRACT

Information about the characteristics of ice particles in clouds is necessary for improving our understanding of the states, processes, and subsequent modeling of clouds and precipitation for numerical weather prediction and climate analysis. Two NASA passive microwave radiometers, the satellite-borne Global Precipitation Measurement (GPM) Microwave Imager (GMI) and the aircraft-borne Conical Scanning Millimeter-Wave Imaging Radiometer (CoSMIR), measure vertically and horizontally polarized microwaves emitted by clouds (including precipitating particles) and Earth's surface below. In this paper, GMI (or CoSMIR) data are analyzed with *CloudSat* (or aircraft-borne radar) data to find polarized difference (PD) signals not affected by the surface, thereby obtaining the information on ice particles. Statistical analysis of 4 years of GMI and *CloudSat* data, for the first time, reveals that optically thick clouds contribute positively to GMI PD at 166 GHz over all the latitudes and their positive magnitude of 166-GHz GMI PD varies little with latitude. This result suggests that horizontally oriented ice crystals in thick clouds are common from the tropics to high latitudes, which contrasts the result of *Cloud–Aerosol Lidar and Infrared Pathfinder Satellite Observations (CALIPSO)* that horizontally oriented ice crystals are rare in optically thin ice clouds.


### 1. Introduction

Ice clouds in the upper troposphere play a crucial role in Earth's radiation balance because of their widespread occurrence and long duration [e.g., Webster and Stephens 1980; Hartmann et al. 1984; Harrison et al. 1993; Zeng et al. 2009; Luo et al. 2017; see Baran (2012) and Yang et al. (2015) for a review]. However, they are not represented well in current weather and climate models (e.g., Zhang et al. 2005; Mace et al. 2009; Jiang et al. 2012; Powell et al. 2012). Field campaign and laboratory observations show that the ice crystals growing from water vapor are usually nonspherical (Pruppacher and Klett 1997). Since ice-crystal shape is important in radiation computation (e.g., Liu et al. 1998; Baran 2012; Yang et al. 2005, 2015), how to observe ice crystal properties (e.g., shape, orientation) is

imperative to parameterize nonspherical ice crystals in climate models.

Observations of ice crystals from aircraft penetrating clouds are expensive and limited to over a few geographic regions. Hence, the remote sensing of ice crystal shape is becoming important (e.g., Sassen 1974; Intrieri et al. 2002; Skofronick-Jackson et al. 2015). In 2014, the Global Precipitation Measurement (GPM) satellite was launched (Hou et al. 2014; Skofronick-Jackson et al. 2015, 2017), where the GPM Microwave Imager (GMI) measures the intensity of radiation (via brightness temperature) at high frequencies (e.g., 166 and 183 GHz) that were added to GMI specifically for observing the properties of ice particles. GMI's microwave polarization data (e.g., 166V, 166H) can be used to analyze the distribution of ice crystal shape and orientation (Skofronick-Jackson et al. 2008; Gong and Wu 2017; Gong et al. 2018).

Since GMI receives the upwelling radiances emitted by both clouds (including precipitating particles) and Earth's surface below, it is interesting to find polarized

 Denotes content that is immediately available upon publication as open access.

Corresponding author: Dr. Xiping Zeng, xiping.zeng.civ@mail.mil

DOI: 10.1175/JCLI-D-18-0293.1

© 2018 American Meteorological Society. For information regarding reuse of this content and general copyright information, consult the AMS Copyright Policy ([www.ametsoc.org/PUBSReuseLicenses](http://www.ametsoc.org/PUBSReuseLicenses)).

difference (PD) signals not affected by the surface. *CloudSat* (Stephens et al. 2002) intersected the GPM core satellite and thus provided additional cloud information to distinguish the contributions of clouds and Earth's surface. In other words, the coincidence data of *CloudSat* and GMI can be used to identify the contribution of clouds to GMI PD, providing information on ice crystal orientation.

Lidar data of backscatter and depolarization from *Cloud–Aerosol Lidar and Infrared Pathfinder Satellite Observations* (CALIPSO) were used to retrieve ice crystal information in optically thin ice clouds, showing that the fraction of thin clouds containing oriented crystals is extremely small (less than 1%) when cloud temperature is below  $-30^{\circ}\text{C}$ , whereas the fraction is 30%–50% and increases with latitude (except in the Antarctic) when cloud temperature is above  $-30^{\circ}\text{C}$  (e.g., Noel and Chepfer 2010; Zhou et al. 2012). In this study, the coincidence data of *CloudSat* and GMI are used to obtain ice crystal information in optically thick ice clouds. Specifically, we utilize the *CloudSat*–GPM coincidence dataset (Turk 2017) to study the spatial distribution of cloud-induced microwave polarization difference, inferring the distribution of ice crystal properties (e.g., ice crystal orientation) in optically thick ice clouds. To support the analysis methodology used, we first analyze the data from the aircraft-borne Conical Scanning Millimeter-Wave Imaging Radiometer (CoSMIR; which functions similarly to GMI) over the Midlatitude Continental Convective Clouds Experiment (MC3E; Jensen et al. 2016).

This study is presented with four sections. In section 2, CoSMIR and radar data from MC3E are analyzed, providing a methodology to analyze the *CloudSat*–GPM coincidence dataset. In section 3, the *CloudSat*–GPM coincidence dataset is analyzed statistically, showing the global distribution of cloud-induced microwave polarization difference. Finally, section 4 gives a summary and discussion.

## 2. Analysis of CoSMIR data from MC3E

In this section, data from CoSMIR and radars over MC3E are analyzed as an example, providing a methodology to analyze GMI data. Passive microwave (PMW) radiometers, including CoSMIR and GMI, measure the upwelling radiances emitted by the atmosphere, clouds, precipitation, and Earth below (e.g., Skofronick-Jackson and Johnson 2011). Their data can be used to retrieve hydrometeor particle information and rain rates (e.g., Kummerow 1993; Olson et al. 2001a; Liu 2004). Since ice crystals in the atmosphere scatter incident microwave radiation, especially at high frequencies ( $>85$  GHz), the

amount of microwaves scattered and thus received by PMW radiometers depends on ice crystals aloft (Skofronick-Jackson et al. 2008). If the ice crystals are nonspherical (e.g., plate like) and oriented with respect to the PMW viewing angle, the microwaves received by PMW radiometers become polarized (e.g., Roberti and Kummerow 1999; Adams et al. 2008). Hence, the difference in radiance between horizontally and vertically polarized channels, especially at high frequencies (e.g., 166 GHz), should indicate the general orientation of ice crystals. Generally speaking, when the GMI brightness temperature  $T_b$  at 166 GHz for vertically polarized microwaves is higher than that for horizontally polarized microwaves, there are horizontally oriented ice crystals aloft (e.g., Roberti and Kummerow 1999; Adams et al. 2008; Defer et al. 2014).

Defining PD as  $\Delta T_b$  (the difference of vertical and horizontal brightness temperatures), a positive PD at 166 GHz implies the existence of horizontally oriented ice crystals, and its magnitude is directly proportional to the percentage of horizontally oriented ice crystals and their size (Roberti and Kummerow 1999; Adams et al. 2008; Defer et al. 2014). Thus, the PD at 166 GHz is analyzed in this paper against the PD at 89 GHz. Note also that a nadir-viewing radiometer should have a PD equal to zero.

CoSMIR and GMI are PMW radiometers with high frequencies and operate with conical scans (thus, at an approximate  $53.6^{\circ}$  viewing angle to the hydrometeors in clouds; Wang et al. 2007, 2008; Draper et al. 2015). CoSMIR has nine channels with frequencies centered at 50.3, 52.8, 89, 165.5,  $183.3 \pm 1$ ,  $183.3 \pm 3$ , and  $183.3 \pm 7$  GHz. (Channels at 89 and 165.5 GHz have both horizontal and vertical polarization; all other channels have only horizontal.) It is loaded on the NASA ER-2 aircraft to observe the atmosphere looking downward with a footprint of  $2.5 \times 4.3 \text{ km}^2$ . Its data from MC3E are analyzed next, providing an analytical procedure for GMI data.

MC3E was a field campaign in south-central Oklahoma conducted in April–June 2011 and jointly led by the NASA GPM Mission and the U.S. Department of Energy's Atmospheric Radiation Measurement (ARM) program (Jensen et al. 2016). In the campaign, CoSMIR and several radars [including the high-altitude imaging wind and rain airborne profile (HIWRAP) radar] were in the high-altitude ER-2 aircraft to measure upwelling microwaves and hydrometeors (Heymsfield et al. 2013).

CoSMIR data from MC3E are analyzed here to show the ice crystal orientation in a mesoscale convective system (MCS). Figure 1 displays the horizontal cross section of radar reflectivity at 10-cm wavelength (or 3-GHz frequency) at an altitude of 3 km at 2234 UTC

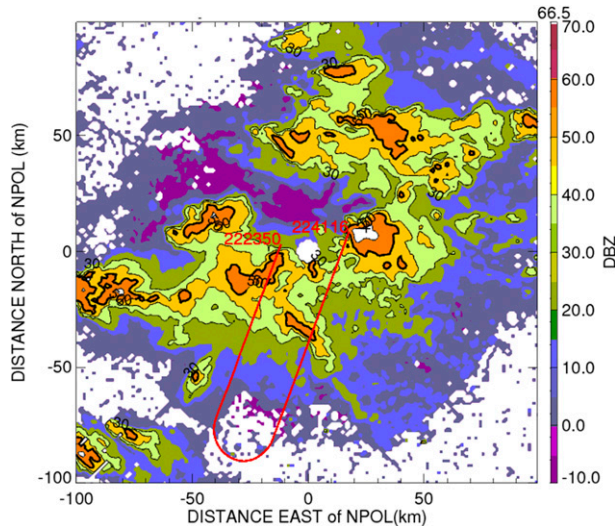


FIG. 1. Horizontal cross section of radar reflectivity at 10-cm wavelength from NPOL at 3-km altitude and 2234 UTC 23 May 2011 during MC3E. Red line shows ER-2 flight track at 2223–2241 UTC 23 May 2011, when the CoSMIR data are analyzed.

23 May 2011 from the ground-based NASA S-Band Dual-Polarimetric Radar (NPOL) located at 36.5°N, 97.2°W. The figure also displays the ER-2 flight track from 2223 to 2241 UTC 23 May 2011. This flight period is chosen for analysis because its observations cover both deep convection and anvil clouds.

The HIWRAP radar and CoSMIR observations in the flight period are analyzed. Figure 2 displays the vertical cross section of Ku-band (2.8-cm wavelength) reflectivity (dBZ) from HIWRAP radar that measures clouds downward, showing there are deep convection, stratiform precipitation, and anvil clouds during the flight period. The figure also displays the PD at 165.5 GHz. Since CoSMIR scans at an off-nadir angle of 53.6°, a distance shift of 5.5 km is applied to the CoSMIR data so that the CoSMIR data in the figure correspond to the radar data below, where  $5.5 \text{ km} \approx (\text{aircraft altitude of } 20 \text{ km} - \text{cloud top altitude of } 10.8 \text{ km}) \times \cos(53.6^\circ)$  (see Fig. 2 for the altitudes used).

Figure 2 shows that the PD at 165.5 GHz is much larger than zero over stratiform clouds and anvil clouds, whereas the PD is only slightly larger than zero over deep convection (Heymsfield and Fulton 1994; Gong and Wu 2017). Such PD suggests the fraction of horizontally oriented ice crystals in nonconvective regions is larger than that in deep convection. Indeed, in deep convection, particles are experiencing updrafts that cause them to rotate almost randomly with no preferred orientation via turbulence and detrain the particles near cloud tops so that they have insufficient time to select their orientation.

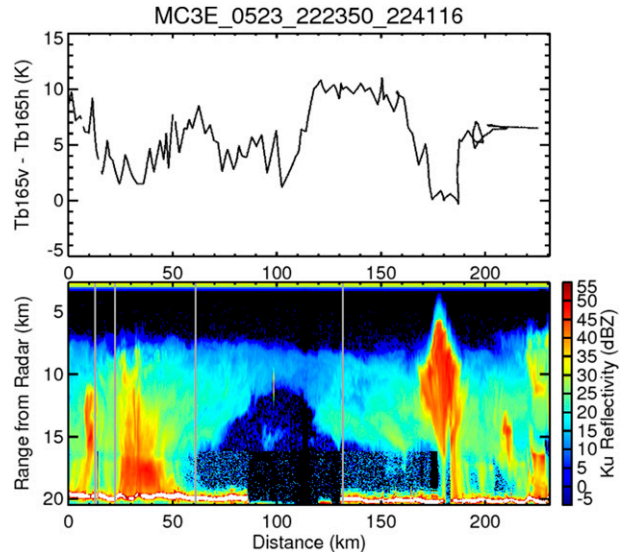


FIG. 2. PD at 165.5 GHz obtained from (top) CoSMIR's conical scan at nadir and (bottom) the reflectivity from HIWRAP's Ku-band (2.8-cm wavelength) measurements along the MC3E flight track (Fig. 1).

### 3. Statistical analysis of the GMI–CloudSat coincidence data

#### a. GMI–CloudSat coincidence data

In this section, 4 years of GMI and *CloudSat* coincidence data are analyzed following the MC3E analysis procedure in section 2 except that GMI and *CloudSat* replace CoSMIR and HIWRAP radar, respectively. GMI (or GPM) and *CloudSat* fly in sun-asynchronous and sun-synchronous orbits, and thus cross each other frequently (e.g., Luo et al. 2017; Turk 2017). Their interactions (or coincidences), with small enough time difference, provide unique observations of clouds and their PD just as CoSMIR and HIWRAP radar in MC3E (or Fig. 2).

GMI flies at an altitude of 407 km and scans with an off-nadir angle of 48.5° (Hou et al. 2014; Skofronick-Jackson et al. 2015). It has swaths of  $\sim 885 \text{ km}$  wide and 13 channels (i.e., 10.6, 18.7, 23.8, 36.5, 89, 166,  $183.3 \pm 3$ ,  $183.3 \pm 7 \text{ GHz}$ ), where channels at 10.6, 18.7, 36.5, 89, and 166 GHz have both horizontal and vertical polarization and all other channels have only vertical. Figure 3 displays two-dimensional (2D) GMI brightness temperature of horizontally polarized microwaves at 36, 89, and 166 GHz over the Amazon on 13 November 2014, where GMI scans are remapped onto 2D planes based on their geographical position.

*CloudSat* uses a 94-GHz (W band) nadir-looking radar or the Cloud Profiling Radar (CPR) to measure clouds below, providing vertical cross sections of radar reflectivity over its ground tracks (Stephens et al. 2002).

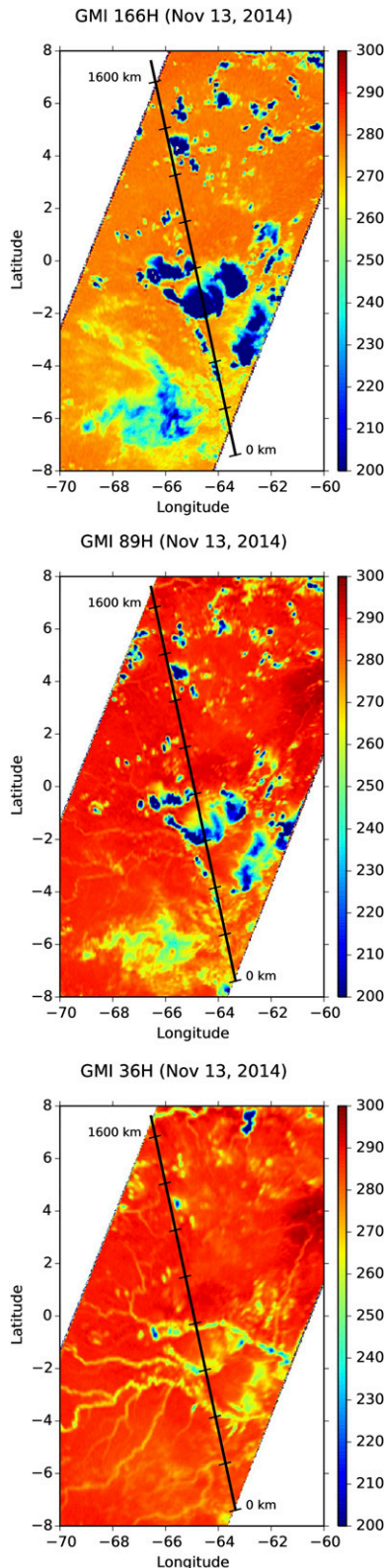


FIG. 3. GMI brightness temperature (K) at (top) 166, (middle) 89 and (bottom) 36 GHz for the horizontal modes over the Amazon at 1806 UTC 13 November 2014. Thick line denotes the *CloudSat* track that heads north, and is scaled with a unit of 200 km.

Figure 3, for example, displays a *CloudSat* ground track on the GMI swaths S1 and S2, where swath S2 has four channels with frequencies 166 GHz and above, and swath S1 has nine channels with frequencies below 166 GHz. Although each CPR beam is not located exactly as a GMI scan, its brightness temperatures are estimated using those of GMI scans that are closest to the CPR beam.

The GPM data product 2B.CSATGPM is used to compile the coincident data of GPM and *CloudSat* [see Turk (2017) for details]. It chooses the intersections between the GMI and *CloudSat* ground tracks, which occurred within  $\pm 15$  min of each other. Since the CPR has a horizontal resolution of  $\sim 1$  km and GMI has a footprint of  $\sim 4.1 \times 6.3$  km<sup>2</sup> at 166 GHz, the brightness temperatures at each CPR beam position take those of GMI scans at the nearest neighbor to avoid any spatial or temporal resampling artifacts (Turk 2017).

The product covers 4732 intersect lines of GPM and *CloudSat* from 8 March 2014 to 25 October 2017. It is analyzed next statistically for the global distribution of PD.

#### b. Case analysis of the 166-GHz PD

One intersect line of the GMI–*CloudSat* coincidence data is analyzed first as an example. Figure 3 displays the GMI brightness temperature of horizontally polarized microwaves at 36, 89, and 166 GHz over the Amazon on 13 November 2014. The figure also displays the track of *CloudSat* that heads north. The brightness temperatures at different frequencies provide a three-dimensional structure of clouds, to some extent, because microwaves with high frequency are more sensitive to small ice crystals than those with low frequency. Hence, the 166H image exhibits the spatial distribution of small ice crystals, showing a big anvil of mesoscale convective systems in the upper troposphere. In contrast, the 89H image exhibits the distribution of relatively large ice crystals, with a relatively small anvil at relatively lower altitude. The 36H image displays information on large ice crystals/drops in convective cores and thick clouds, with little information on cloud anvil. Meanwhile, the 36H image contains the signal of the surface such as branches of the Amazon River, which can be verified with the Google map of the river.

*CloudSat* crossed the GPM-core satellite orbit shown in Fig. 3. Figure 4 displays the vertical cross section of *CloudSat* radar reflectivity and the GMI PD at 166 GHz (or  $\Delta T_b = 166V - 166H$ ) along the same *CloudSat* track. The figure suggests PD is positive over thick clouds but close to zero over thin cirrus clouds in the tropics (near distance 1000 km). This does not necessarily mean that thin cirrus ice particles are not in an oriented state, rather that they are likely too small to be sensed by the 166-GHz channels. Note that PD is close to 10 K in stratiform cloud

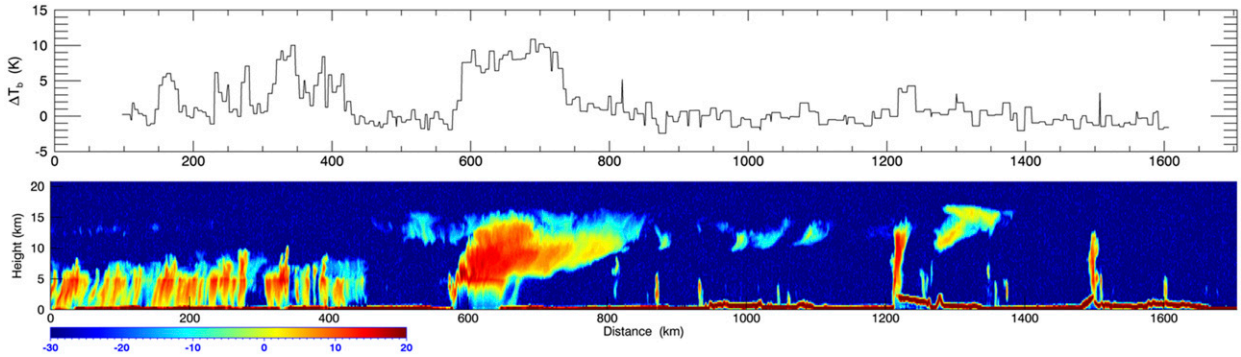


FIG. 4. Vertical cross section of the (bottom) *CloudSat* radar reflectivity and (top) GMI PD ( $\Delta T_b = 166V - 166H$ ) along the same *CloudSat* track (see Fig. 3) when both *CloudSat* and GPM flew over the Amazon. Dataset starts over 7.38°S, 63.35°W at 1805:45 UTC and ends over 7.6°N, 66.55°W at 1806:52 UTC 13 November 2014.

regions where it is expected that ice particles are not subject to the turbulence in convective regions and thus can remain in a relatively fixed orientation. This nearly 10-K difference was also true for the CoSMIR data.

It seems that Figs. 4 and 2 (GMI and CoSMIR, respectively) have different PD magnitudes over deep convection, which can be understood from two sides. First, the 36-GHz brightness temperature in Fig. 3 indicates that the strong radar reflectivity at  $\sim 630$  km in Fig. 4 is at the edge of deep convective cores rather than right over core centers. Hence, the upward transport of randomly oriented ice crystals by convective updrafts may not affect the GMI PD at  $\sim 630$  km in Fig. 4.

Second, the CoSMIR footprint of  $2.5 \times 4.3 \text{ km}^2$  is smaller than the GMI one of  $4.1 \times 6.3 \text{ km}^2$ , and therefore CoSMIR is more sensitive to the spatial variation in PD than GMI. Since convective updrafts are small scale and usually embedded in mesoscale cloud systems, CoSMIR can catch the contribution of convective updrafts on GMI PD better than GMI, which may partly explain the small difference in GMI PD between convective and thick clouds in Fig. 5.

#### c. Statistical analysis of the 166-GHz PD

The statistical analysis of GMI data supports the PD results obtained from the preceding cases. To show the

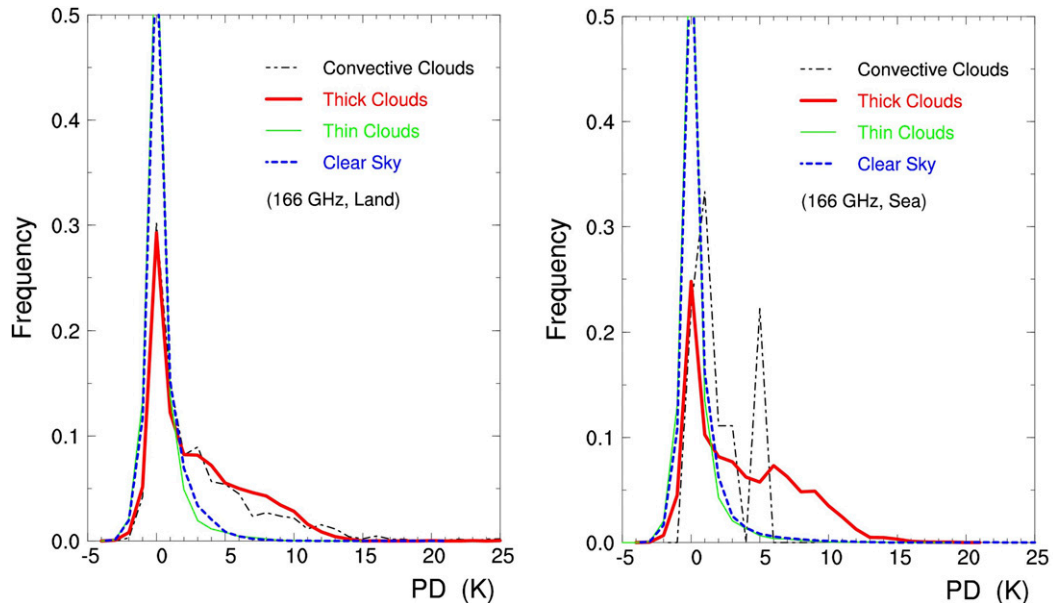


FIG. 5. PDF of GMI PD  $\Delta T_b$  at 166 GHz over (left) land and (right) sea in the tropics. Black, red, green, and blue lines represent atmospheric columns (or pixels) with the maximum radar reflectivity above 20 dBZ (deep convective clouds), between 5 and 20 dBZ (thick clouds), between  $-20$  and 5 dBZ (thin clouds), and below  $-20$  dBZ (clear sky and extremely thin clouds), respectively.

sensitivity of PD to latitude, clouds, and the underlying surface, atmospheric columns (or pixels) are classified into four categories: large drops in deep convective, moderate drops in thick, small drops in thin, and extremely thin clouds (including diamond dust and clear-sky cases) when the maximum *CloudSat* radar reflectivity above 3 km is larger than 20 dBZ, between 5 and 20 dBZ, between  $-20$  and 5 dBZ, and less than  $-20$  dBZ, respectively. These categories are somewhat related to the optical depth of the clouds and precipitation, but herein we use thickness as our category titles. The thicknesses are further distinguished by their underlying surface of sea and land. Finally, the thicknesses are divided into three geographical zones or latitudes lower than  $25^\circ$ , between  $25^\circ$  and  $50^\circ$ , and higher than  $50^\circ$  in both hemispheres.

The thresholds of  $-20$ , 5, and 20 dBZ are chosen with the following consideration. Roughly speaking, the GMI 166-GHz channel can sense clouds with maximum radar reflectivity above  $\sim 5$  dBZ. Hence, 5 dBZ is used to separate all cases into two parts: sensible and nonsensible cases. Of all the sensible cases, 20 dBZ is used to distinguish deep convection from other thick clouds, addressing the statistical difference in PD between convective and stratiform clouds (just like the difference shown in Fig. 2). Of all the nonsensible cases,  $-20$  dBZ is used to distinguish thin clouds from extremely thin clouds (or clear sky). Since the 166-GHz channel cannot sense thin clouds, it is predicted that the statistics of PD over thin clouds and clear sky are affected only by Earth's surface and therefore should be close to each other, which is used to test the present statistics method (e.g., its sample/pixel number and the threshold of 5 dBZ). As shown in the following paragraphs, the 166-GHz PD statistics over thin clouds is close to that over clear sky, which suggests the threshold of 5 dBZ is reasonable.

With the classification of atmospheric columns (or pixels), the data of GMI and *CloudSat* are analyzed for the probability distribution function (PDF) of PD at 166 GHz in the tropics first. Figure 5 displays PDFs of tropical PD over four kinds of clouds. PDFs over the thin (both continental and oceanic) clouds are close to those over the extremely thin clouds (or clear sky), indicating the 166-GHz channel cannot sense the thin clouds. In other words, the PD over thin clouds comes mainly from the underlying surface (Adams et al. 2008) and thus is also treated as the background here for brevity.

Figure 5 also shows that the PD over thick clouds is significantly larger than that over thin clouds (or background distribution), exhibiting a positive contribution of thick clouds to the PD. Specifically, thick clouds bring about an additional PD increase of

$\sim 6$  K in the tropics. Such positive contribution of thick clouds to 166-GHz PD indicates that thick clouds prefer a horizontally aligned orientation of ice crystals.

Deep convective clouds, as shown in Fig. 5, contribute positively to 166-GHz PD, too, but less than thick clouds, which supports the case analyses in Fig. 2. In addition, the PDF of PD over oceanic convective clouds exhibits two peaks at 1.5 and 5.5 K, which may be associated with convective upward transport of randomly oriented ice crystals and other crystal-orientation processes only for stratiform clouds. Moreover, the difference in 166-GHz PD between oceans and land may correspond to their difference in the diurnal variation of 166-GHz PD, where the 166-GHz PD has a strong diurnal variation over land but not over oceans (Gong et al. 2018).

Figure 6 shows the latitudinal variation of 166-GHz PD by displaying the PDFs of PD over thick and extremely thin clouds (or clear sky, referred to here as background) in the low, middle, and high latitudes. The PDF for clear sky originates in the radiative emission of Earth's surface. Its meridional variation shows that the 166-GHz PD of the surface's radiation increases with latitude and the increase in the PD with latitude is stronger over sea than over land.

The PDF with clouds has two main contributors: cloud/precipitation particles and Earth's surface. Thus, the contribution of clouds is inferred by subtracting the PDF for clear sky from that with clouds. Hence, Fig. 6 shows that thick clouds contribute positively to the 166-GHz PD in all of the latitudes. In summary, the positive contribution of thick clouds to the 166-GHz PD exists in all the latitudes and has no obvious meridional tendency, which indicates thick clouds prefer a horizontally aligned orientation of ice crystals from the tropics to high latitudes.

#### d. Analysis of the 89-GHz PD

If all horizontally oriented ice crystals had the same size, their number concentration could be estimated using only the GMI PD at 166 GHz. However, ice crystals usually have different sizes. Hence, retrieving the number concentration of oriented crystals at different sizes needs additional information on PD at other frequencies. In short, 89-GHz PD is sensitive to relatively large ice crystals, whereas 166-GHz PD is sensitive to relatively small ones. In this subsection, GMI PD at 89 GHz is analyzed, exploring the potential application of 89-GHz PD for orientation retrieval of relatively large ice crystals.

Figure 7 displays the PDFs of PD at 89 GHz with thick cloud and clear sky over land and sea in the low, middle

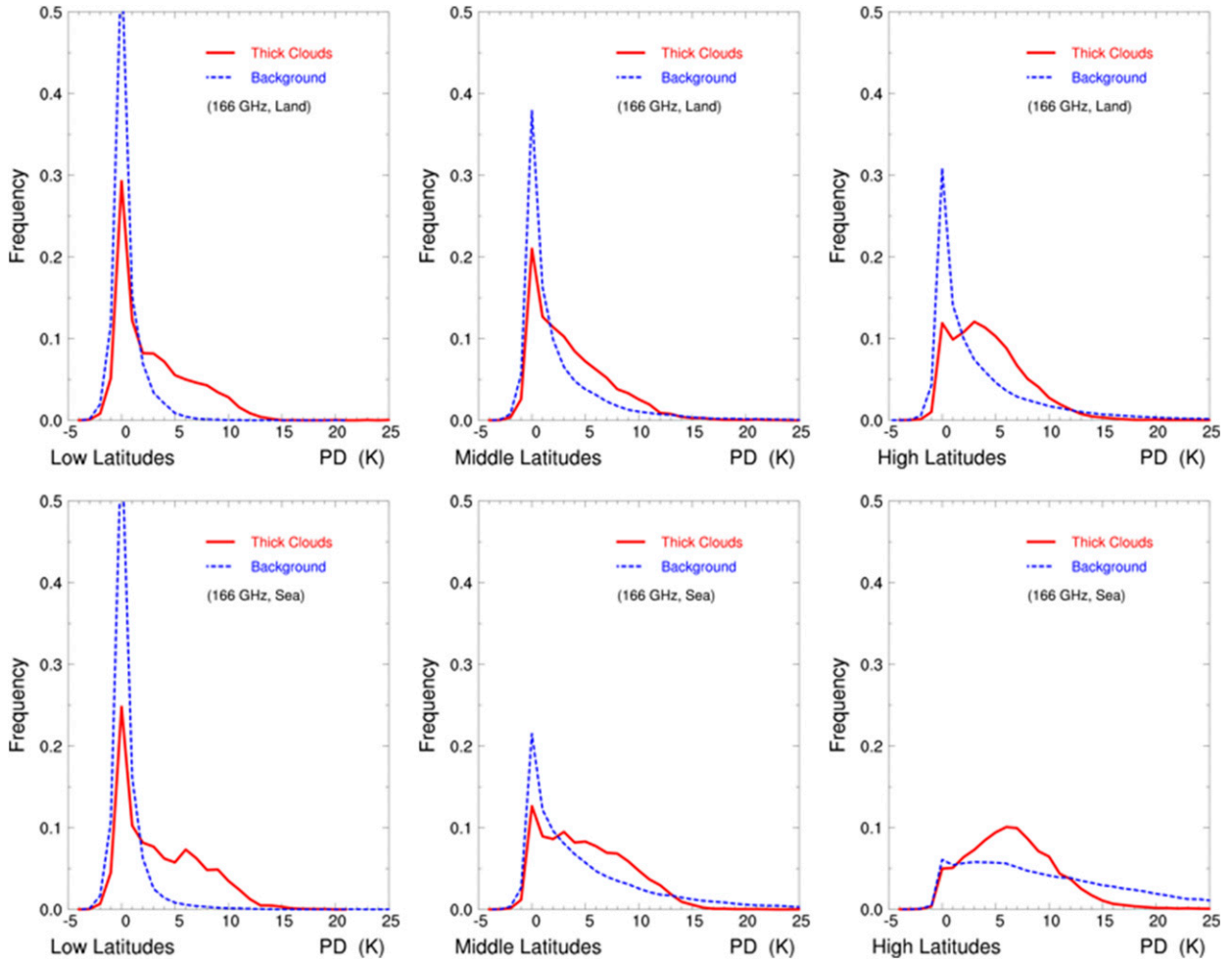


FIG. 6. PDF of GMI PD  $\Delta T_b$  at 166 GHz over (top) land and (bottom) sea vs latitude. Thick lines represent columns with the maximum radar reflectivity at 5–20 dBZ and thin ones the maximum radar reflectivity below  $-20$  dBZ (referred to here as background) in the (left) low, (center) middle, and (right) high latitudes.

and high latitudes, respectively. The 89-GHz PD emitted by the underlying surface, different from the counterpart at 166 GHz, is quite large especially over sea. As a result, the 89-GHz PD over thick clouds is relatively small, which is reasonable because a large amount of spherical (or randomly oriented) hydrometeors in the lower part of thick clouds depolarize the upwelling background (polarized) microwaves (Adams et al. 2008).

Since the microwave radiation from the underlying surface is highly polarized at 89 GHz, it is difficult to infer the contribution of ice clouds to 89-GHz PD based on the GMI observations. However, light rain would make the liquid precipitation layer almost opaque and unpolarized at 89 GHz. It is estimated with physics modeling that the PD over a calm ocean surface with a 4-km-deep liquid precipitation layer is  $\sim 0.1$  K at 166 GHz

and  $\sim 3$  K at 89 GHz for a weak rain rate of  $\sim 2$  mm  $h^{-1}$ , although the PD varies considerably with atmospheric humidity, sea surface wind, and other cloud parameters. Hence, if an 89-GHz footprint is filled with light rain with ice-phase precipitation above it, then the PD is still an indication of the polarizing effect of the ice-phase precipitation (Olson et al. 2001b).

The application of 89-GHz PD to cloud analysis is illustrated using the case in Fig. 3. Figure 8 displays the GMI PD images at 89 and 166 GHz for the case. The 166-GHz PD image shows a spatial distribution of clouds similar to the 166H image, containing little surface signal. The 89-GHz PD image catches clouds well, although it contains some surface signal (e.g., branches of the Amazon River). However, the surface signal can be identified easily using its high 89H  $T_b$  in Fig. 3. In brief, the 89-GHz PD provides an additional variable to

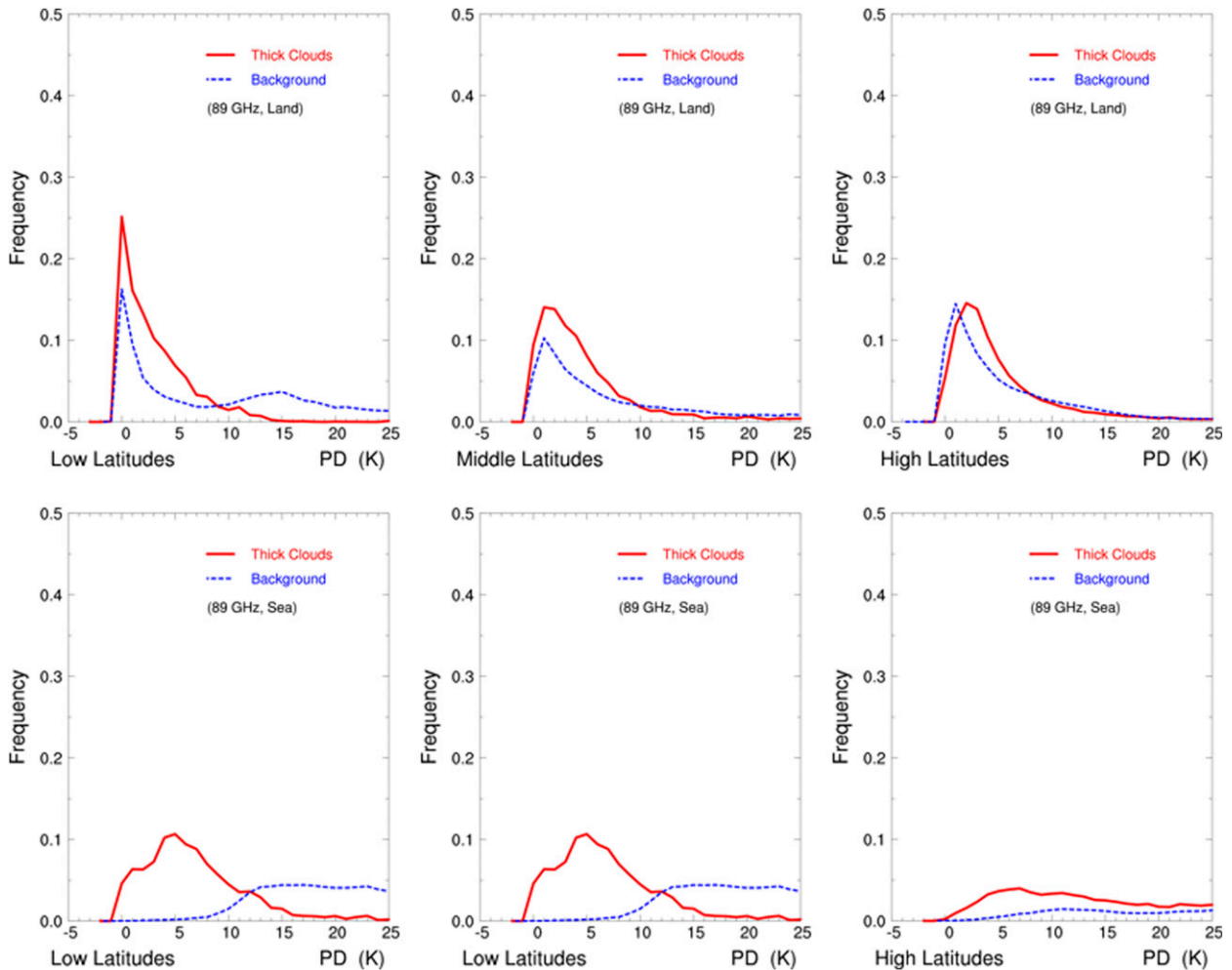


FIG. 7. As in Fig. 6, but for the radiation at 89 GHz.

retrieve ice crystal properties in mixed-phase clouds (or the clouds with liquid water below).

#### 4. Conclusions and discussion

##### a. Summary of the PD analysis

The microwave polarization data from CoSMIR and GMI are analyzed for the global distribution of PD at high frequencies (i.e., 89 and 166 GHz) with the following remarks:

- The analysis methodology of CoSMIR and radar data over MC3E is extended to the GMI and *CloudSat* coincidence data for the global distribution of cloud-induced PD at the high frequencies. It is found that the results from CoSMIR and GMI are consistent.
- Four years of GMI and *CloudSat* coincidence data reveal that the thick clouds with maximum radar reflectivity between 5 and 20 dBZ contribute positively

to the 166-GHz PD by  $\sim 6$  K, suggesting that horizontally oriented ice crystals in the thick clouds are common from the tropics to high latitudes.

- The coincidence data also show that the microwave radiation from the underlying surface is highly polarized at 89 GHz especially over sea, suggesting that the 89-GHz GMI PD is suitable to study the ice process precipitation in mixed-phase clouds, but not in ice clouds.

##### b. Discussion of the PD characteristics

The present result of positive GMI 166-GHz PD over thick clouds can be used to infer the physics of ice crystal orientation. It is well known that the dynamics of ice crystals prefers horizontal orientation of ice crystals in quiet air (Pruppacher and Klett 1997, p. 445). If this process dominated ice crystal orientation in thick clouds, horizontally oriented ice crystals would prevail



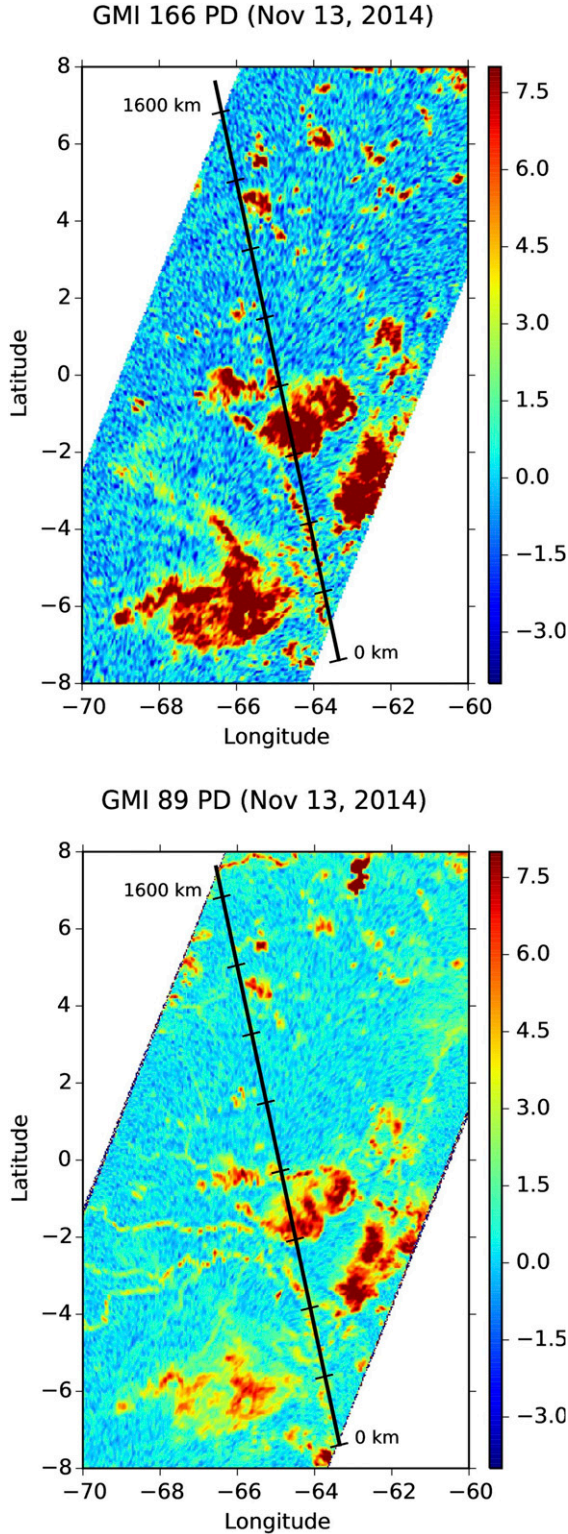


FIG. 8. As in Fig. 3, but for the images of GMI PD (K) at (top) 166 and (bottom) 89 GHz.

and thus bring about a positive PD, which is consistent with the present result of GMI PD.

However, the deduction of positive PD works well only if its condition of “quiet air” is satisfied. In fact, quiet air is rare in thick clouds, and atmospheric (even background) turbulence can disrupt an orientation order that ice crystals would otherwise possess, bringing about no preferred orientation of ice crystals, especially small ones (see Fig. 2 for the small 166-GHz PD over turbulent deep convection; Klett 1995; Pruppacher and Klett 1997, p. 610). Based on the present result of positive 166-GHz PD and the orientation model of Klett (1995), it is inferred that small ice crystals in thick clouds are oriented randomly because of turbulence, whereas large ones are oriented horizontally with no obvious effect of turbulence.

On the other side, the magnitude of positive 166-GHz PD depends on the number and size of horizontally oriented large ice crystals. Statistical analysis of GMI PD data revealed a strong diurnal variation of 166-GHz PD over tropical land (Gong et al. 2018), suggesting a diurnal variation of horizontally oriented ice crystals in number and/or size.

The diurnal variation of horizontal oriented ice crystals in number and size is caused by the conversion of randomly oriented small ice crystals to horizontally oriented large ones. Hence, the variation can be explained by the radiative effect on microphysics (REM) that is responsible for dew/frost and its diurnal variation (e.g., Heymsfield 1973; Hall and Pruppacher 1976; Stephens 1983; Wu et al. 2000; Zeng 2008).

REM is classified with the radiative ratio (Zeng 2008, 2018a,b)

$$\eta_z = \frac{F^+ + F^-}{2\sigma T^4}, \quad (1)$$

where  $\sigma$  is the Stefan–Boltzmann constant,  $T$  is air temperature, and  $F^+$  and  $F^-$  denote the upward and downward fluxes of infrared radiation in the atmosphere, respectively. When  $\eta_z < 1$  (or the condition for dew/frost formation), ice crystals undergo radiative cooling and thus large ice crystals grow at the expense of small ones; when  $\eta_z > 1$ , ice crystals undergo radiative warming, which brings about no large ice crystals if there is no upward motion (Zeng 2008, 2018a,b).

In an air parcel with  $\eta_z < 1$ , horizontally oriented ice crystals lose energy more efficiently to space by infrared radiation than other crystals, because the former have larger area faced to space than the latter. As a result, horizontally oriented ice crystals have lower crystal temperature than other crystals and consequently water vapor prefers to deposit on the former, accelerating the conversion of randomly oriented small ice crystals to horizontally oriented large ones (Zeng et al. 2016; Zeng 2018b).

Since a strong diurnal variation of land surface temperature can lead to a diurnal variation of  $\eta_z$  via  $F^+$ , infrared and solar radiation brings about a diurnal variation of REM (Zeng 2018a) that in turn leads to a diurnal variation of horizontally oriented ice crystals in number and size over land, which is consistent with the observed diurnal variation of GMI 166-GHz PD over land (Gong et al. 2018).

Furthermore, REM partly explains the positive GMI PD over thick clouds. Consider a thick cloud. Since its lower part blocks the large upwelling infrared radiation emitted by the land/sea,  $F^+$  near the cloud top is decreased, bringing about  $\eta_z < 1$  and thus an increase of horizontally oriented ice crystals in number and size there (Heymsfield 1973; Zeng 2008), which is consistent with the present result of positive 166-GHz PD over thick clouds.

In summary, the present observational study and Gong et al. (2018) suggest there are other processes of oriented ice crystals (e.g., REM) besides the ice crystal dynamics that contribute to GMI PD. To quantitatively compare the contributions of REM and the ice crystal dynamics to GMI PD, an ice crystal–orientation model will be developed that incorporates REM, the effect of ice crystal dynamics (Klett 1995), and other cloud processes. A specific connection between model output and satellite-observed variables (e.g., brightness temperature) will be built for a quantitative interpretation of GMI and other similar satellite data.

*Acknowledgments.* The authors are grateful to Dr. R. Kakar at NASA headquarters for his support of this research. They would like to thank Dr. Joe Turk for providing the coincident data of GMI and *CloudSat*. They thank Drs. Gerry Heymsfield and James Wang as well as HIWRAP and CoSMIR engineering teams for data-processing and engineering support. Special thanks are given to the three anonymous reviewers for their constructive comments. This research was supported by the NASA Precipitation Measurement Mission (PMM) project under Grant NNX16AE24G. It was also supported by the NASA *CloudSat*/CALIPSO project under Grant NNX16AM06G.

## REFERENCES

- Adams, I. S., P. Gaiser, and W. L. Jones, 2008: Simulation of the Stokes vector in inhomogeneous precipitation. *Radio Sci.*, **43**, RS5006, <https://doi.org/10.1029/2007RS003744>.
- Baran, A. J., 2012: From the single-scattering properties of ice crystals to climate prediction: A way forward. *Atmos. Res.*, **112**, 45–69, <https://doi.org/10.1016/j.atmosres.2012.04.010>.
- Defer, E., V. S. Galligani, C. Prigent, and C. Jimenez, 2014: First observations of polarized scattering over ice clouds at close-to-millimeter wavelengths (157 GHz) with MADRAS on board the Megha-Tropiques mission. *J. Geophys. Res. Atmos.*, **119**, 12301–12316, <https://doi.org/10.1002/2014JD022353>.
- Draper, D. W., D. A. Newell, F. J. Wentz, S. Krimchansky, and G. Skofronick-Jackson, 2015: The Global Precipitation Measurement (GPM) Microwave Imager (GMI): Instrument overview and early on-orbit performance. *IEEE J. Sel. Top. Appl. Earth Obs. Remote Sens.*, **8**, 3452–3462, <https://doi.org/10.1109/JSTARS.2015.2403303>.
- Gong, J., and D. L. Wu, 2017: Microphysical properties of frozen particles inferred from Global Precipitation Measurement (GPM) Microwave Imager (GMI) polarimetric measurements. *Atmos. Chem. Phys.*, **17**, 2741–2757, <https://doi.org/10.5194/acp-17-2741-2017>.
- , X. Zeng, D. L. Wu, and X. Li, 2018: Diurnal variation of tropical ice cloud microphysics: Evidence from Global Precipitation Measurement Microwave Imager (GPM-GMI) polarimetric measurements. *Geophys. Res. Lett.*, **45**, 1185–1193, <https://doi.org/10.1002/2017GL075519>.
- Hall, W. D., and H. R. Pruppacher, 1976: The survival of ice particles falling from cirrus clouds in subsaturated air. *J. Atmos. Sci.*, **33**, 1995–2006, [https://doi.org/10.1175/1520-0469\(1976\)033<1995:TSOIPF>2.0.CO;2](https://doi.org/10.1175/1520-0469(1976)033<1995:TSOIPF>2.0.CO;2).
- Harrison, E. F., P. Minnis, B. R. Barkstrom, and G. G. Gibson, 1993: Radiation budget at the top of the atmosphere. *Atlas of Satellite Observations Related to Global Change*, R. J. Gurney, J. L. Foster, and C. L. Parkinson, Eds., Cambridge University Press, 19–38.
- Hartmann, D. L., H. H. Hendon, and R. A. Houze Jr., 1984: Some implications of the mesoscale circulations in tropical cloud clusters for large-scale dynamics and climate. *J. Atmos. Sci.*, **41**, 113–121, [https://doi.org/10.1175/1520-0469\(1984\)041<0113:SIOTMC>2.0.CO;2](https://doi.org/10.1175/1520-0469(1984)041<0113:SIOTMC>2.0.CO;2).
- Heymsfield, A. J., 1973: Cirrus uncinus generating cells and the evolution of cirriform clouds. Ph.D. thesis, University of Chicago, 273 pp.
- Heymsfield, G. M., and R. Fulton, 1994: Passive microwave and infrared structure of mesoscale convective systems. *Meteor. Atmos. Phys.*, **54**, 123–139, <https://doi.org/10.1007/BF01030055>.
- , L. Tian, L. Li, M. McLinden, and J. I. Cervantes, 2013: Airborne radar observations of severe hailstorms: Implications for future spaceborne radar. *J. Appl. Meteor. Climatol.*, **52**, 1851–1867, <https://doi.org/10.1175/JAMC-D-12-0144.1>.
- Hou, A. Y., and Coauthors, 2014: The Global Precipitation Measurement Mission. *Bull. Amer. Meteor. Soc.*, **95**, 701–722, <https://doi.org/10.1175/BAMS-D-13-00164.1>.
- Intrieri, J. M., M. D. Shupe, T. Uttal, and B. J. McCarty, 2002: An annual cycle of Arctic cloud characteristics observed by radar and lidar at SHEBA. *J. Geophys. Res.*, **107**, 8030, <https://doi.org/10.1029/2000JC000423>.
- Jensen, M. P., and Coauthors, 2016: The Midlatitude Continental Convective Clouds Experiment (MC3E). *Bull. Amer. Meteor. Soc.*, **97**, 1667–1686, <https://doi.org/10.1175/BAMS-D-14-00228.1>.
- Jiang, J. H., and Coauthors, 2012: Evaluation of cloud and water vapor simulations in CMIP5 climate models using NASA “A-Train” satellite observations. *J. Geophys. Res.*, **117**, D14105, <https://doi.org/10.1029/2011JD017237>; Corrigendum, **118**, 11 087, <https://doi.org/10.1002/jgrd.50864>.
- Klett, J. D., 1995: Orientation model for particles in turbulence. *J. Atmos. Sci.*, **52**, 2276–2285, [https://doi.org/10.1175/1520-0469\(1995\)052<2276:OMFPIT>2.0.CO;2](https://doi.org/10.1175/1520-0469(1995)052<2276:OMFPIT>2.0.CO;2).
- Kummerow, C., 1993: On the accuracy of the Eddington approximation for radiative transfer in the microwave frequencies. *J. Geophys. Res.*, **98**, 2757–2765, <https://doi.org/10.1029/92JD02472>.

- Liu, G., 2004: Approximation of single scattering properties of ice and snow particles for high microwave frequencies. *J. Atmos. Sci.*, **61**, 2441–2456, [https://doi.org/10.1175/1520-0469\(2004\)061<2441:AOSSPO>2.0.CO;2](https://doi.org/10.1175/1520-0469(2004)061<2441:AOSSPO>2.0.CO;2).
- Liu, Y., W. P. Arnott, and J. Hallett, 1998: Anomalous diffraction theory for arbitrarily oriented finite circular cylinders and comparisons with exact *T*-matrix results. *Appl. Opt.*, **37**, 5019–5030, <https://doi.org/10.1364/AO.37.005019>.
- Luo, Z. J., R. C. Anderson, W. B. Rossow, and H. Takahashi, 2017: Tropical cloud and precipitation regimes as seen from near-simultaneous TRMM, CloudSat, and CALIPSO observations and comparison with ISCCP. *J. Geophys. Res. Atmos.*, **122**, 5988–6003, <https://doi.org/10.1002/2017JD026569>.
- Mace, G. G., Q. Zhang, M. Vaughan, R. Marchand, G. Stephens, C. Trepte, and D. Winker, 2009: A description of hydrometeor layer occurrence statistics derived from the first year of merged Cloudsat and CALIPSO data. *J. Geophys. Res.*, **114**, D00A26, <https://doi.org/10.1029/2007JD009755>.
- Noel, V., and H. Chepfer, 2010: A global view of horizontally oriented crystals in ice clouds from Cloud-Aerosol Lidar and Infrared Pathfinder Satellite Observation (CALIPSO). *J. Geophys. Res.*, **115**, D00H23, <https://doi.org/10.1029/2009JD012365>.
- Olson, W. S., P. Bauer, C. D. Kummerow, Y. Hong, and W.-K. Tao, 2001a: A melting-layer model for passive/active microwave remote sensing applications. Part II: Simulation of TRMM observations. *J. Appl. Meteor.*, **40**, 1164–1179, [https://doi.org/10.1175/1520-0450\(2001\)040<1164:AMLMFP>2.0.CO;2](https://doi.org/10.1175/1520-0450(2001)040<1164:AMLMFP>2.0.CO;2).
- , Y. Hong, C. D. Kummerow, and J. Turk, 2001b: A texture-polarization method for estimating convective-stratiform precipitation area coverage from passive microwave radiometer data. *J. Appl. Meteor.*, **40**, 1577–1591, [https://doi.org/10.1175/1520-0450\(2001\)040<1577:ATPMFE>2.0.CO;2](https://doi.org/10.1175/1520-0450(2001)040<1577:ATPMFE>2.0.CO;2).
- Powell, S. W., R. A. Houze Jr., A. Kumar, and S. A. McFarlane, 2012: Comparison of simulated and observed continental tropical anvil clouds and their radiative heating profiles. *J. Atmos. Sci.*, **69**, 2662–2681, <https://doi.org/10.1175/JAS-D-11-0251.1>.
- Pruppacher, H. R., and J. D. Klett, 1997: *Microphysics of Clouds and Precipitation*. Kluwer, 954 pp.
- Roberti, L., and C. Kummerow, 1999: Monte Carlo calculations of polarized microwave radiation emerging from cloud structures. *J. Geophys. Res.*, **104**, 2093–2104, <https://doi.org/10.1029/1998JD200038>.
- Sassen, K., 1974: Depolarization of laser light backscattered by artificial clouds. *J. Appl. Meteor.*, **13**, 923–933, [https://doi.org/10.1175/1520-0450\(1974\)013<0923:DOLLBB>2.0.CO;2](https://doi.org/10.1175/1520-0450(1974)013<0923:DOLLBB>2.0.CO;2).
- Skofronick-Jackson, G., and B. T. Johnson, 2011: Surface and atmospheric contributions to passive microwave brightness temperatures for falling snow events. *J. Geophys. Res.*, **116**, D02213, <https://doi.org/10.1029/2010JD014438>.
- , A. Heymsfield, E. Holthaus, C. Albers, and M.-J. Kim, 2008: Nonspherical and spherical characterization of ice in Hurricane Erin for wideband passive microwave comparisons. *J. Geophys. Res.*, **113**, D06201, <https://doi.org/10.1029/2007JD008866>; Corrigendum, **113**, D14210, <https://doi.org/10.1029/2008JD010387>.
- , and Coauthors, 2015: Global Precipitation Measurement Cold Season Precipitation Experiment (GCPEX): For measurement's sake, let it snow. *Bull. Amer. Meteor. Soc.*, **96**, 1719–1741, <https://doi.org/10.1175/BAMS-D-13-00262.1>.
- , and Coauthors, 2017: Global Precipitation Measurement (GPM) mission for science and society. *Bull. Amer. Meteor. Soc.*, **98**, 1679–1695, <https://doi.org/10.1175/BAMS-D-15-00306.1>.
- Stephens, G. L., 1983: The influence of radiative transfer on the mass and heat budgets of ice crystals falling in the atmosphere. *J. Atmos. Sci.*, **40**, 1729–1739, [https://doi.org/10.1175/1520-0469\(1983\)040<1729:TIORTO>2.0.CO;2](https://doi.org/10.1175/1520-0469(1983)040<1729:TIORTO>2.0.CO;2).
- , and Coauthors, 2002: The *CloudSat* mission and the A-Train: A new dimension to space-based observations of clouds and precipitation. *Bull. Amer. Meteor. Soc.*, **83**, 1771–1790, <https://doi.org/10.1175/BAMS-83-12-1771>.
- Turk, J., 2017: CloudSat-GPM coincidence dataset, version 2A. NASA Tech. Memo., 23 pp., [https://pps.gsfc.nasa.gov/Documents/CSATGPM\\_COIN\\_ATBD.pdf](https://pps.gsfc.nasa.gov/Documents/CSATGPM_COIN_ATBD.pdf).
- Wang, J. R., P. E. Racette, J. R. E. Piepmeier, B. Monosmith, and W. Manning, 2007: Airborne CoSMIR observations between 50 and 183 GHz over snow-covered Sierra Mountains. *IEEE Trans. Geosci. Remote Sens.*, **45**, 55–61, <https://doi.org/10.1109/TGRS.2006.885410>.
- , —, and —, 2008: A comparison of near concurrent measurements from the SSMIS and CoSMIR for some selected channels over the frequency range of 50–183 GHz. *IEEE Trans. Geosci. Remote Sens.*, **46**, 923–933, <https://doi.org/10.1109/TGRS.2007.904038>.
- Webster, P. J., and G. L. Stephens, 1980: Tropical upper-tropospheric extended clouds: Inferences from winter MONEX. *J. Atmos. Sci.*, **37**, 1521–1541, <https://doi.org/10.1175/1520-0469-37.7.1521>.
- Wu, T., W. R. Cotton, and W. Y. Y. Cheng, 2000: Radiative effects on the diffusional growth of ice particles in cirrus clouds. *J. Atmos. Sci.*, **57**, 2892–2904, [https://doi.org/10.1175/1520-0469\(2000\)057<2892:REOTDG>2.0.CO;2](https://doi.org/10.1175/1520-0469(2000)057<2892:REOTDG>2.0.CO;2).
- Yang, P., H. Wei, H.-L. Huang, B. A. Baum, Y. X. Hu, G. W. Kattawar, M. I. Mishchenko, and Q. Fu, 2005: Scattering and absorption property database for nonspherical ice particles in the near- through far-infrared spectral region. *Appl. Opt.*, **44**, 5512–5523, <https://doi.org/10.1364/AO.44.005512>.
- , K.-N. Liou, L. Bi, C. Liu, B. Yi, and B. A. Baum, 2015: On the radiative properties of ice clouds: Light scattering, remote sensing, and radiation parameterization. *Adv. Atmos. Sci.*, **32**, 32–63, <https://doi.org/10.1007/s00376-014-0011-z>.
- Zeng, X., 2008: The influence of radiation on ice crystal spectrum in the upper troposphere. *Quart. J. Roy. Meteor. Soc.*, **134**, 609–620, <https://doi.org/10.1002/qj.226>.
- , 2018a: Modeling the effect of radiation on warm rain initiation. *J. Geophys. Res. Atmos.*, **123**, 6896–6906, <https://doi.org/10.1029/2018JD028354>.
- , 2018b: Radiatively induced precipitation formation in diamond dust. *J. Adv. Model. Earth Syst.*, **10**, 2300–2317, <https://doi.org/10.1029/2018MS001382>.
- , and Coauthors, 2009: A contribution by ice nuclei to global warming. *Quart. J. Roy. Meteor. Soc.*, **135**, 1614–1629, <https://doi.org/10.1002/qj.449>.
- , G. Skofronick-Jackson, L. Tian, A. E. Emory, W. S. Olson, and R. A. Kroodsma, 2016: Analysis of the GMI/CoSMIR microwave polarization data for ice crystal modeling. *2016 Precipitation Measurement Mission (PMM) Meeting*, Houston, Texas, NASA, <https://pmm.nasa.gov/meetings/all/2016-pmm-science-team-meeting>.
- Zhang, M. H., and Coauthors, 2005: Comparing clouds and their seasonal variations in 10 atmospheric general circulation models with satellite measurements. *J. Geophys. Res.*, **110**, D15S02, <https://doi.org/10.1029/2004JD005021>.
- Zhou, C., P. Yang, A. E. Dessler, Y. Hu, and B. A. Baum, 2012: Study of horizontally oriented ice crystals with CALIPSO observations and comparison with Monte Carlo radiative transfer simulations. *J. Appl. Meteor. Climatol.*, **51**, 1426–1439, <https://doi.org/10.1175/JAMC-D-11-0265.1>.